

Computational exploration of a viable route to Kitaev-quantum spin liquid phase in OsCl_3

Qiangqiang Gu,^{1,2} Shishir Kumar Pandey,^{2,*} and Yihao Lin³

¹*School of Mathematical Science, Peking University, Beijing 100871, China*

²*AI for Science Institute, Beijing, China*

³*International Center for Quantum Materials, School of Physics, Peking University, Beijing 100871, China*

(Dated: April 11, 2023)

In this computational study, we explore a viable route to access the Kitaev-Quantum Spin Liquid (QSL) state in a so-called spin-orbit assisted Mott insulator OsCl_3 . QSL state is stabilized in a substantial part of the Hubbard U -Hund's J_H space of the quantum phase diagram obtained by combining second-order perturbation and pseudo-Fermion renormalization group calculations. Considering monolayer of recently synthesized OsCl_3 as a case study, we show that for small J_H/U , only Kitaev interaction appears, albeit of smaller magnitude. Depending upon the nature of magnetic interactions, the phase diagram also hosts other magnetic phases as well in different regions. Negligibly small farther neighbor interactions appears as a distinct feature of monolayer OsCl_3 . Insights from our study may be helpful in designing experiments on pertinent Kitaev-QSL candidate materials.

The Kitaev honeycomb model with bond-dependent Ising-type exchange interactions on a honeycomb lattice naturally hosts the novel quantum spin liquid (QSL) state [1]. The realization of the Kitaev model in so-called spin-orbit coupling (SOC) assisted Mott insulators was proposed by Jackeli and Khaliullin [2]. This requires SOC active transition-metal ions to be in edge-shared octahedral crystal field (CF) of anions, and Sr_2IrO_4 was initially proposed as an example [2]. Since then, many materials like $\alpha\text{-RuCl}_3$ [3–7] and Cobaltates [8–18], other Iridates [19–26] are proposed as pertinent Kitaev-QSL candidates [27, 28]. In these materials, the formation of $j_{\text{eff}} = 1/2$ Kramers doublets, which form the low-energy space in the materials, results from the interplay of octahedral CF (Δ^{CF}) and SOC. Although the dominant magnetic interaction between these pseudospin $1/2$ states is proposed to be Kitaev (K) type [2], other *undesirable* interactions such as isotropic Heisenberg (J) and off-diagonal terms (Γ), as well as farther neighbor couplings, also appear, causing long-range magnetic order in the aforementioned materials, and driving them away from a possible QSL ground state.

Despite such inevitable challenges in real materials, attempts have been made to access the QSL state using external knobs. For example, magnetic interactions in $\alpha\text{-RuCl}_3$ were manipulated by means of the external magnetic field to achieve the QSL state [29–31]. In another theoretical attempt by Liu *et. al.* [11], $\Delta_{\text{tr}}^{\text{CF}}$ was proposed as a tunable parameter with pressure to realize QSL state in Cobaltates. Towards this goal, our computational study in this article aims to explore the Kitaev-QSL state in SOC-assisted Mott insulators through manipulation of the fundamental electronic parameters U and J_H . Our study is also motivated in part by recent

theoretical work that argues for the experimental tuning of U and J_H parameters in perovskites with epitaxial strain, based on advancements in experimental epitaxial growth techniques [32].

To realize our goal, we consider the OsCl_3 monolayer as a case study. Our material choice is based on the fact it satisfies all the necessary criterion mentioned earlier to host strong Kitaev interactions, *viz* $\text{Os}^{+3} 5d^5$ ions in the edge-shared OsCl_6 octahedron possess large SOC interaction. In a recent experimental study by Kataoka *et. al.* [33], magnetization and heat capacity measurements on $\text{Os}_{0.81}\text{Cl}_3$ revealed the absence of any long-range magnetic ordering of Os^{+3} spins arranged on the triangular lattice (with local honeycomb domain formation) up to 0.08 K temperature, which can be an indication of underlying strong magnetic frustration in this compound, also a building block for Kitaev physics. A previous computational attempt to study the topological properties of this compound proposed a ferromagnetic (FM) ground state for the monolayer OsCl_3 [34], but a scrupulous investigation of its magnetic properties is warranted in the light of the fact that the iso-electronic $\alpha\text{-RuCl}_3$ has a zigzag (ZZ) antiferromagnetic (AFM) ground state. From computational modeling perspective, electronic parameters U and J_H are part of Hubbard-Kanamori H_{int} Hamiltonian in Eq. S4. The full model Hamiltonian \mathcal{H} in Eq. S4 has been quite successful and hence, widely accepted for estimation of magnetic interactions in these materials [7, 17, 35–37]. Hence, one can explore the access to the Kitaev-QSL phase by tuning the U and J_H parameters and calculating the corresponding magnetic interactions which is the objective of this article.

We first used *ab initio* calculations of higher accuracy to show that the ZZ and FM configurations in this material are nearly degenerate, indicating highly competing magnetic interactions that may be a reason for the absence of long-range magnetic ordering in this compound. We then varied U and J_H/U in the second or-

* shishir.kr.pandey@gmail.com

der perturbation calculations to obtain magnetic interactions and input them into pseudofermion functional renormalization-group (pf-FRG) calculations, which allowed us to obtain a U - J_H/U quantum phase diagram. At small values of J_H/U , we found the emergence of only K -type first nearest neighbor (1NN) interaction, albeit of smaller magnitude, resulting in the Kitaev-QSL state occupying a substantial part of the phase diagram. In addition to the QSL state, we also find FM, ZZ, and Néel states present in different parts of the phase diagram. Interestingly, we find that the second and third neighbor magnetic interactions are negligibly smaller in monolayer OsCl_3 , which suggests that this material might be a better candidate for the exploration of possible QSL state than the previously proposed Iridates, α - RuCl_3 and Cobaltates.

Crystal structure and magnetism – ab initio calculations: We consider the $C2/m$ honeycomb crystal structure of the monolayer OsCl_3 which is similar to α - RuCl_3 [34, 38]. Very recently, triangular lattice with nanometer sized honeycomb domains of Os atoms has been observed experimentally [33]. The structure is shown in Fig. 1(a) and Fig. S1 of supplementary material (SM) [39]. The full optimization of lattice constants within highly accurate *ab initio* calculations after imposition of both ZZ and FM state brings nearly identical crystal structure in both cases. Our phonon calculations with this optimized crystal structure indicate that the honeycomb lattice of OsCl_3 monolayer is at least dynamically stable. Details of *ab initio* calculations, optimized crystal structure, and phonon calculations can be found in Sec. S1 of SM [39].

To understand the nature of magnetism and underlying frustration, highly accurate *ab initio* total energy calculations are performed, with tighter energy and force convergence criterion, after imposing various magnetic configurations like FM, ZZ, Néel and Stripe. We varied U on Os d states in the range 0.1–3 eV and the SOC effect is self-consistently included. The results, shown in Fig. 1(b) reveal that the ZZ state is lowest in energy when the spins are canted in an out-of-plane direction towards the center of one of the Cl-Cl edges in an OsCl_6 octahedron (see Fig. 1(a)), with the closely competing FM state higher in energy. Other AFM configurations like Néel and stripe are energetically much higher. Such orientation of magnetic moments was also proposed for Na_2IrO_3 [40, 41]. The energy difference between the ZZ and FM state nearly vanishes for the in-plane arrangement of spins along the a axis as shown in Fig. 1(d). This is consistent with the previous study by Sheng *et al.* [34]. The nearly degenerate FM and ZZ configurations, which differ by a single 1NN spin flip, are indicative of large magnetic frustration present in the system, explaining the absence of long-range magnetic ordering observed in experiment [33]. Larger energy difference between other AFM states, like Néel and stripe, and ZZ state may indicate that the exchange interactions in monolayer OsCl_3 may not be weak. In most simplis-

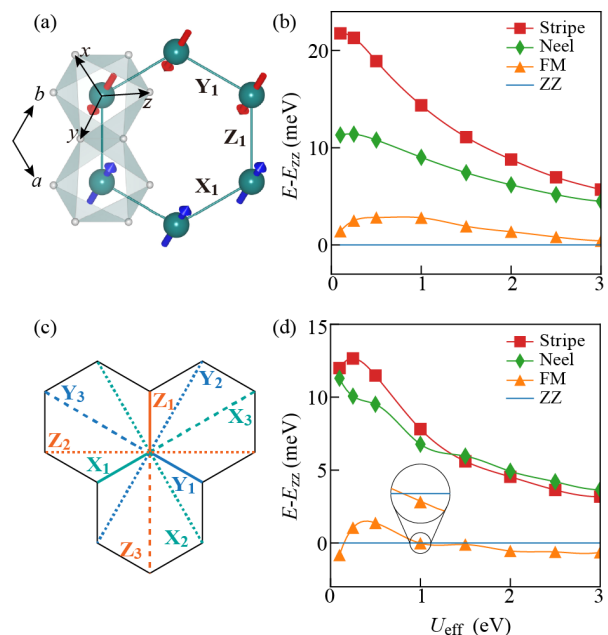


FIG. 1. (a) Top view of out-of-plane spin arrangement on a hexagon in ZZ magnetic state in monolayer OsCl_3 . Spins point towards the center of one of the Cl-Cl edges in an OsCl_6 octahedron. Big Cyan and small gray balls represent Os and Cl atoms; x , y and z are local axes while a and b are crystallographic axes. Variation of the total energy of different magnetic configurations relative to ZZ state with U on Os d states for, (b) out-of-plane spin alignment, and (d) alignment of spins along a axis. (c) Color-coded X, Y, and Z bonds upto 3NN are shown.

tic second-order perturbation theory, magnetic exchange interactions are $\propto t^2/U$ at large U values if one treats hopping t as a perturbation. The expected $1/U$ behavior [42, 43] of magnetic stability curves in Fig. 1 (b) and (d) at large values U is apparent. We also find that the in-plane magnetic anisotropy for monolayer OsCl_3 is quite small (see Fig. S3 of SM [39]). Next, we describe the electronic Hamiltonian considered in this study for exploration of U - J_H quantum phase diagram in the quest of QSL state.

Model Hamiltonian: The full Hamiltonian for d^5 systems is given as [7, 17, 35, 36],

$$\mathcal{H} = H_{\text{hop}} + H_{\text{cf}} + H_{\text{soc}} + H_{\text{int}} \quad (1)$$

where terms in right hand side are hopping, CF, SOC and Hubbard-Kanamori Hamiltonians, respectively. For Mott insulators, in limit $t \ll U$, one can separate the “onsite” term H_i^0 from \mathcal{H} . H_i^0 , represented in basis $\psi_{i\sigma}^\dagger = [d_{z2}^\dagger, d_{xz}^\dagger, d_{yz}^\dagger, d_{x^2-y^2}^\dagger, d_{xy}^\dagger]_{i\sigma}$ for site i and spin σ , then

reads as,

$$\begin{aligned}
H_i^0 &= H_{\text{cf}} + H_{\text{soc}} + H_{\text{int}} \\
&= \sum_{i,\sigma} \psi_{i\sigma}^\dagger \Delta_i^{\text{CF}} \psi_{i\sigma} + \sum_i \lambda \mathbf{L}_i \cdot \mathbf{s}_i \\
&+ \frac{U}{2} \sum_{i,\alpha} n_{i\alpha\sigma} n_{i\alpha\sigma'} + \frac{U'}{2} \sum_{i,\alpha \neq \beta} n_{i\alpha} n_{i\beta} \\
&- \frac{J_{\text{H}}}{2} \sum_{i,\sigma,\sigma',\alpha \neq \beta} \psi_{i\alpha\sigma}^\dagger \psi_{i\alpha\sigma'} \psi_{i\beta\sigma'}^\dagger \psi_{i\beta\sigma} \\
&- \frac{J'}{2} \sum_{i,\sigma \neq \sigma',\alpha \neq \beta} \psi_{i\alpha\sigma}^\dagger \psi_{i\beta\sigma'} \psi_{i\alpha\sigma'}^\dagger \psi_{i\beta\sigma} \quad (2)
\end{aligned}$$

In above expression, U/U' are intraorbital/interorbital Coulomb interaction terms, and J_{H} and J' are Hund's coupling and pair hopping interaction, respectively. Rotational invariance in the isolated atom limit dictates the relationships: $U' = U - 2J_{\text{H}}$ and $J_{\text{H}} = J'$. Δ_i^{CF} and hopping amplitudes t_{ij} in $H_{\text{hop}} = \sum_{i \neq j, \sigma} \psi_{i\sigma}^\dagger T_{ij} \psi_{j\sigma}$ are obtained from a Wannier based tight-binding (TB) model excluding SOC effect. Strength of SOC in monolayer OsCl_3 , $\lambda = 0.355$ eV, is estimated by a band-structure fitting procedure (see Sec S2 [39] for details). As proposed earlier, it might be possible to experimentally tune parameters U and J_{H} by epitaxial strain in advance growth techniques [32]. Hence, we vary these two parameters to explore for possibility of QSL state in monolayer OsCl_3 . For a d^5 system, dimension of Hilbert spaces for H_i^0 is $C_5^{10} = 252$ and by exactly diagonalizing it, we obtain the lowest two eigenstates as the $j_{\text{eff}} = 1/2$ Kramers doublet. We then use second-order perturbation method, treating hopping as perturbation, to estimate magnetic interactions between these pseudo-spin states. Details of the methodology and discussions on validity of low-energy $j_{\text{eff}} = 1/2$ picture and atomic features which can be observed in experiments for monolayer OsCl_3 are presented in Sec. S3, S4 and S6 of SM [39].

Magnetic interactions and quantum phase diagram: Estimated magnetic interactions up to 3NN (Fig. 1(c) depicts bonds up to 3NN) from second-order perturbation method are used as input for the pf-FRG calculations. We then analyzed the ground states by plotting the static spin correlation function, obtained from pf-FRG calculations, in the first and extended BZ of monolayer OsCl_3 . Our choice of pf-FRG method as a quantum toolkit is based on its earlier demonstrated success in exploring quantum phase diagrams on different lattice and spin models [44, 45]. Our obtained quantum phase diagram for a range of U (0.5 - 3.0 eV) and J_{H}/U (0.075 - 0.3) is shown in Fig. 2(a). This range of parameters is chosen so that the phase space is extended on either side of the point $U = 1.7$ eV and $J_{\text{H}} = 0.3$ eV ($J_{\text{H}}/U \sim 0.176$) previously considered for $5d$ system such as Iridates in the literature [35]. Details of pf-FRG calculations are given in Sec. S5 of SM [39]. We will now discuss this phase diagram in detail.

Various magnetic phases *viz* FM, ZZ and Néel and

TABLE I. Estimated bond-dependent magnetic interactions for monolayer OsCl_3 using second-order perturbation method at $U = 1.7$ eV, $J_{\text{H}} = 0.3$ eV and $\lambda = 0.355$ eV. Values of Heisenberg J , Kitaev K , off-diagonal Γ , Γ' and asymmetric DMI \mathbf{D} terms along with diagonal and off-diagonal anisotropic terms ξ and ζ are listed. 3NN interactions as well as some 2NN interactions are < 0.05 meV and hence not listed here.

Bond	Magnetic interactions (meV)					
	J	K	Γ	Γ'	ξ	ζ
X ₁	0.220	-19.993	-5.711	0.858	1.342	-1.940
Y ₁	0.115	-19.203	-5.755	-1.096	-0.767	-2.577
Z ₁	0.144	-19.214	5.299	3.516	-1.295	0.382
X ₂	-0.211	0.573	-0.137	-0.056	-	-0.088
Y ₂	-0.230	0.633	-0.126	0.074	-	-0.167
Z ₂	-0.234	0.636	0.115	0.144	-	0.061
\mathbf{D}_{ij}						
X ₂	(-0.073, -0.190, 0.172)					
Y ₂	(0.183, -0.184, -0.060)					
Z ₂	(0.166, -0.050, 0.199)					

QSL states occupy different parts of the phase diagram. At smaller value of $U = 0.5$ eV and $J_{\text{H}}/U = 0.075 - 0.15$, there is a (< 1.5 meV) 1NN FM J which is slightly larger than the AFM K coupling resulting in an FM ground state with a competing ZZ phase. This behavior manifested in star-like shape of static spin susceptibility (hereafter only susceptibility) plot in Fig. 2(c) (last plot). Consistent with the FM phase, major contribution to the susceptibility comes from the zone center while small spreads along M -points in the first BZ indicates a competing ZZ AFM phase. Transition to latter happens when both couplings change their respective signs with FM $K >$ AFM J , which is consistency with a recent observation on Cobaltates [17]. At a typical phase point $U = 0.5$ eV and $J_{\text{H}}/U = 0.1$ in this region, depicted by white star in Fig. 2(a), we obtained $J = -0.5$ meV $K = 0.35$ meV.

Away from FM-ZZ phase boundary, other terms like Γ , Γ' , ξ , ζ as well as smaller farther neighbor interactions started to emerge in ZZ region of the phase diagram. However, 1NN dominant K and J terms remain FM and AFM, respectively. We emphasize here that 2NN and 3NN interactions are at least 2 \sim 3 order of magnitude smaller than 1NN and have no qualitative effect on the magnetic ground state. Values of $U = 1.7$ eV and $J_{\text{H}} = 0.3$ eV brings ZZ state (white star in ZZ region in Fig. 2(a)) and estimated interactions are listed in Table I. Corresponding susceptibility plot in Fig. 2(c) (second from the left) has dominant contributions from M -points of the first BZ, consistent with the underlying ZZ magnetic order. In the absence of inversion symmetry on the 2NN bonds, a small Dzyaloshinskii-Moriya interaction (DMI) appears for these magnetic neighbors. We would like to mention that the value of U and J_{H} obtained from cRPA calculations also brings a ZZ state, details of

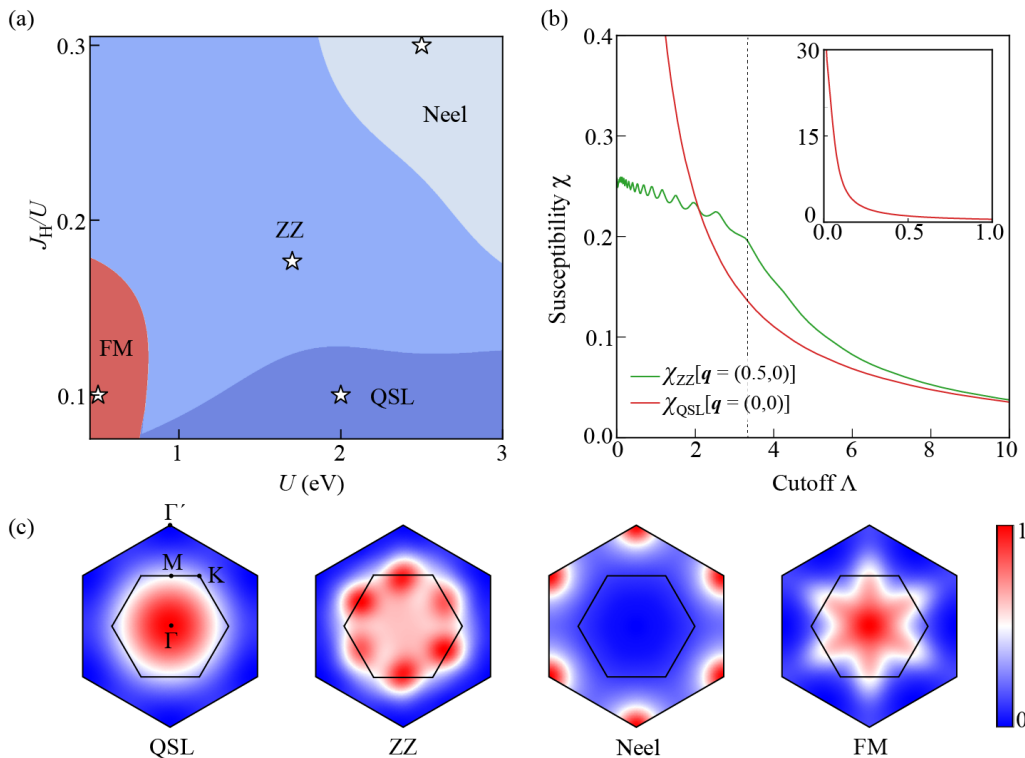


FIG. 2. (a) Magnetic quantum phase diagram in U - J_H/U parameter space obtained using a combination of second-order perturbation and pf-FRG calculations. The range considered is $U = 0.5 - 3.0$ eV and $J_H/U = 0.075 - 0.3$ are considered. Obtained magnetic phases are FM, ZZ, Néel and QSL magnetic states. Static spin correlations plots in (c) correspond to the points depicted by star symbols in (a). Intensity is normalized for each plot in (c), and the inner and outer hexagon in these plots denote first and extended BZ of monolayer OsCl_3 . (b) The renormalization group flow of the magnetic correlations (χ) for the two cases, ZZ (green curve) and QSL (red) states with inset showing the flow at low frequencies for QSL state. Vertical dash line show the break of flow of χ for ZZ state while its smooth flow for QSL state indicative of no spontaneous symmetry breaking.

which is provided in Sec. S7 of SM [39]. ZZ phase occupying largest part of the phase diagram quantitatively differ in different regions and a related discussion is provided in Sec. S7 of SM [39]. Further increase of U ($\approx 2 - 3$ eV) and J_H/U ($\approx 0.2 - 0.3$) stabilizes Néel AFM state, with 1NN AFM J being the dominant interaction while all other interactions are highly suppressed. For a typical phase point $U = 2.5$ eV, $J_H/U = 0.3$ (marked by white star in Néel region), 1NN, 2NN and 3NN J values are 3.39, 0.39 and 0.03 meV, respectively. Contribution from Γ' points of the extended BZ in the corresponding susceptibility plot shown in Fig. 2(c) (third from the left) is consistent with the underlying Néel magnetic order.

Most importantly, a substantial region of phase diagram, in range of $U = 1.0 - 3.0$ eV, $J_H/U = 0.075 - 0.1$, is occupied by Kitaev-QSL state. In this region, we only obtained small but finite 1NN FM K term (~ 1 meV) in our second-order perturbation calculations. The susceptibility plot for this state shown in Fig. 2(c) (left most) has contribution from the whole first BZ, with highest intensity appearing at the Γ point. No long-range magnetic ordering and hence, no spontaneous symmetry breaking is expected for this state even at low temperatures. To

verify this, we can plot renormalization group flow of the magnetic correlations (χ) as a function of renormalization group cutoff (Λ). Spontaneous symmetry breaking by onset of a long-range magnetic ordering at a Λ results in a kink or break of χ . Such a plot is shown in Fig. 2(b). The smooth evolution of χ down to lowest Λ can be seen for the QSL state represented by the red curve (see also the inset). For comparison, we also show a similar plot for the ZZ order (green curve) corresponding to interactions listed in Table I. Clearly, χ in this case display a breakdown at $\Lambda_c \approx 3.3$ signaling onset of the ZZ order.

Several remarks are in order. First, though off-diagonal magnetic coupling (e.g. Γ) is large compared to Iridates [35], orders of magnitude smaller farther neighbor magnetic interactions (3NN interactions are all $< |0.05|$) distinguishes monolayer OsCl_3 these earlier proposed Kitaev-QSL candidates including Iridates [17, 35]. Second, strain as an external knob, proposed in Ref. [32] for tuning U and J_H can also be utilized to tune trigonal distortions as suggested in Ref. [11] which can also alter the hopping amplitudes between d orbitals. Hence, it would be interesting to probe the role of strain in tuning the magnetic properties of these QSL candidate materi-

als. Third, tuning of U and J_H to access the QSL region in the phase diagram can also be achieved through choice of suitable elements from periodic table. Advancement in material synthesis techniques can be of great help here.

In conclusion, considering recently synthesized monolayer OsCl_3 as an example, we have explored a route to access Kitaev QSL state by varying U and J_H . These two parameters purportedly can be tuned experimentally with epitaxial strain. Using highly accurate *ab initio* total energy calculations, we show that the ZZ and FM are nearly degenerate indicating the large magnetic frustration which might be the possible reason behind absence of long range magnetic ordering in this material. Combining second-order perturbation and pf-FRG calculations, we presented a magnetic quantum phase diagram in U - J_H/U space. A substantial part this phase diagram hosts

Kitaev QSL state, stabilized by 1NN Kitaev interaction only, with other magnetic phases like FM, ZZ and Néel AFM states also appearing in different region of the phase diagram stabilized by changing dominant magnetic interactions. Insights obtained from our study may be helpful in designing experiments on pertinent Kitaev-QSL candidate materials.

ACKNOWLEDGMENTS

QG and SKP contributed equally to this work. SKP gratefully acknowledges valuable feedback from Prof. D. D. Sarma.

-
- [1] A. Kitaev, Anyons in an exactly solved model and beyond, *Ann. Phys.* **321**, 2 (2006), january Special Issue.
- [2] G. Jackeli and G. Khaliullin, Mott Insulators in the Strong Spin-Orbit Coupling Limit: From Heisenberg to a Quantum Compass and Kitaev Models, *Phys. Rev. Lett.* **102**, 017205 (2009).
- [3] K. W. Plumb, J. P. Clancy, L. J. Sandilands, V. V. Shankar, Y. F. Hu, K. S. Burch, H.-Y. Kee, and Y.-J. Kim, α - RuCl_3 : A spin-orbit assisted Mott insulator on a honeycomb lattice, *Phys. Rev. B* **90**, 041112 (2014).
- [4] R. D. Johnson, S. C. Williams, A. A. Haghighirad, J. Singleton, V. Zapf, P. Manuel, I. I. Mazin, Y. Li, H. O. Jeschke, R. Valentí, and R. Coldea, Monoclinic crystal structure of α - RuCl_3 and the zigzag antiferromagnetic ground state, *Phys. Rev. B* **92**, 235119 (2015).
- [5] A. Banerjee, C. A. Bridges, J.-Q. Yan, A. A. Aczel, L. Li, M. B. Stone, G. E. Granroth, M. D. Lumsden, Y. Yiu, J. Knolle, S. Bhattacharjee, D. L. Kovrizhin, R. Moessner, D. A. Tennant, D. G. Mandrus, and S. E. Nagler, Proximate Kitaev quantum spin liquid behaviour in a honeycomb magnet, *Nat. Mat.* **15**, 733 (2016).
- [6] H.-S. Kim, V. S. V., A. Catuneanu, and H.-Y. Kee, Kitaev magnetism in honeycomb RuCl_3 with intermediate spin-orbit coupling, *Phys. Rev. B* **91**, 241110 (2015).
- [7] W. Wang, Z.-Y. Dong, S.-L. Yu, and J.-X. Li, Theoretical investigation of magnetic dynamics in α - RuCl_3 , *Phys. Rev. B* **96**, 115103 (2017).
- [8] H. Liu and G. Khaliullin, Pseudospin exchange interactions in d^7 cobalt compounds: Possible realization of the Kitaev model, *Phys. Rev. B* **97**, 014407 (2018).
- [9] R. Sano, Y. Kato, and Y. Motome, Kitaev-Heisenberg Hamiltonian for high-spin d^7 Mott insulators, *Phys. Rev. B* **97**, 014408 (2018).
- [10] M. Songvilay, J. Robert, S. Petit, J. A. Rodriguez-Rivera, W. D. Ratcliff, F. Damay, V. Balédent, M. Jiménez-Ruiz, P. Lejay, E. Pachoud, A. Hadj-Azzem, V. Simonet, and C. Stock, Kitaev interactions in the Co honeycomb antiferromagnets $\text{Na}_3\text{Co}_2\text{SbO}_6$ and $\text{Na}_2\text{Co}_2\text{TeO}_6$, *Phys. Rev. B* **102**, 224429 (2020).
- [11] H. Liu, J. c. v. Chaloupka, and G. Khaliullin, Kitaev Spin Liquid in $3d$ Transition Metal Compounds, *Phys. Rev. Lett.* **125**, 047201 (2020).
- [12] L. Viciu, Q. Huang, E. Morosan, H. Zandbergen, N. Greenbaum, T. McQueen, and R. Cava, Structure and basic magnetic properties of the honeycomb lattice compounds $\text{Na}_2\text{Co}_2\text{TeO}_6$ and $\text{Na}_3\text{Co}_2\text{SbO}_6$, *J. Solid State Chem.* **180**, 1060 (2007).
- [13] G. Xiao, Z. Xia, W. Zhang, X. Yue, S. Huang, X. Zhang, F. Yang, Y. Song, M. Wei, H. Deng, and D. Jiang, Crystal Growth and the Magnetic Properties of $\text{Na}_2\text{Co}_2\text{TeO}_6$ with Quasi-Two-Dimensional Honeycomb Lattice, *Cryst. Growth Des.* **19**, 2658 (2019).
- [14] E. Lefrançois, M. Songvilay, J. Robert, G. Nataf, E. Jordan, L. Chaix, C. V. Colin, P. Lejay, A. Hadj-Azzem, R. Ballou, and V. Simonet, Magnetic properties of the honeycomb oxide $\text{Na}_2\text{Co}_2\text{TeO}_6$, *Phys. Rev. B* **94**, 214416 (2016).
- [15] A. K. Bera, S. M. Yusuf, A. Kumar, and C. Ritter, Zigzag antiferromagnetic ground state with anisotropic correlation lengths in the quasi-two-dimensional honeycomb lattice compound $\text{Na}_2\text{Co}_2\text{TeO}_6$, *Phys. Rev. B* **95**, 094424 (2017).
- [16] S. M. Winter, Magnetic couplings in edge-sharing high-spin d^7 compounds, *Journal of Physics: Materials* **5**, 045003 (2022).
- [17] S. K. Pandey and J. Feng, Spin interaction and magnetism in cobaltate kitaev candidate materials: An ab initio and model hamiltonian approach, *Phys. Rev. B* **106**, 174411 (2022).
- [18] W. Chen, X. Li, Z. Hu, Z. Hu, L. Yue, R. Sutarto, F. He, K. Iida, K. Kamazawa, W. Yu, X. Lin, and Y. Li, Spin-orbit phase behavior of $\text{Na}_2\text{Co}_2\text{TeO}_6$ at low temperatures, *Phys. Rev. B* **103**, L180404 (2021).
- [19] J. c. v. Chaloupka, G. Jackeli, and G. Khaliullin, Kitaev-Heisenberg Model on a Honeycomb Lattice: Possible Exotic Phases in Iridium Oxides $A_2\text{IrO}_3$, *Phys. Rev. Lett.* **105**, 027204 (2010).
- [20] Y. Singh, S. Manni, J. Reuther, T. Berlijn, R. Thomale, W. Ku, S. Trebst, and P. Gegenwart, Relevance of the Heisenberg-Kitaev Model for the Honeycomb Lattice Iridates $A_2\text{IrO}_3$, *Phys. Rev. Lett.* **108**, 127203 (2012).
- [21] Y. Singh and P. Gegenwart, Antiferromagnetic Mott insulating state in single crystals of the honeycomb lattice material Na_2IrO_3 , *Phys. Rev. B* **82**, 064412 (2010).

- [22] S. K. Choi, R. Coldea, A. N. Kolmogorov, T. Lancaster, I. I. Mazin, S. J. Blundell, P. G. Radaelli, Y. Singh, P. Gegenwart, K. R. Choi, S.-W. Cheong, P. J. Baker, C. Stock, and J. Taylor, Spin Waves and Revised Crystal Structure of Honeycomb Iridate Na_2IrO_3 , *Phys. Rev. Lett.* **108**, 127204 (2012).
- [23] A. Biffin, R. D. Johnson, S. Choi, F. Freund, S. Manni, A. Bombardi, P. Manuel, P. Gegenwart, and R. Coldea, Unconventional magnetic order on the hyperhoneycomb Kitaev lattice in $\beta\text{-Li}_2\text{IrO}_3$: Full solution via magnetic resonant x-ray diffraction, *Phys. Rev. B* **90**, 205116 (2014).
- [24] A. Biffin, R. D. Johnson, I. Kimchi, R. Morris, A. Bombardi, J. G. Analytis, A. Vishwanath, and R. Coldea, Noncoplanar and Counterrotating Incommensurate Magnetic Order Stabilized by Kitaev Interactions in $\gamma\text{-Li}_2\text{IrO}_3$, *Phys. Rev. Lett.* **113**, 197201 (2014).
- [25] B. H. Kim, G. Khaliullin, and B. I. Min, Electronic excitations in the edge-shared relativistic Mott insulator: Na_2IrO_3 , *Phys. Rev. B* **89**, 081109 (2014).
- [26] H. Gretarsson, J. P. Clancy, X. Liu, J. P. Hill, E. Bozin, Y. Singh, S. Manni, P. Gegenwart, J. Kim, A. H. Said, D. Casa, T. Gog, M. H. Upton, H.-S. Kim, J. Yu, V. M. Katukuri, L. Hozoi, J. van den Brink, and Y.-J. Kim, Crystal-Field Splitting and Correlation Effect on the Electronic Structure of A_2IrO_3 , *Phys. Rev. Lett.* **110**, 076402 (2013).
- [27] L. Clark and A. H. Abdeldaim, Quantum spin liquids from a materials perspective, *Annual Review of Materials Research* **51**, 495 (2021).
- [28] H. Takagi, T. Takayama, G. Jackeli, G. Khaliullin, and S. E. Nagler, Concept and realization of kitaev quantum spin liquids, *Nature Reviews Physics* **1**, 264 (2019).
- [29] S.-H. Baek, S.-H. Do, K.-Y. Choi, Y. S. Kwon, A. U. B. Wolter, S. Nishimoto, J. van den Brink, and B. Büchner, Evidence for a field-induced quantum spin liquid in $\alpha\text{-ruCl}_3$, *Phys. Rev. Lett.* **119**, 037201 (2017).
- [30] J. S. Gordon, A. Catuneanu, E. S. Sørensen, and H.-Y. Kee, Theory of the field-revealed Kitaev spin liquid, *Nat. Commun.* **10**, 2470 (2019).
- [31] L. Janssen and M. Vojta, Heisenberg–kitaev physics in magnetic fields, *Journal of Physics: Condensed Matter* **31**, 423002 (2019).
- [32] B. Kim, P. Liu, J. M. Tomczak, and C. Franchini, Strain-induced tuning of the electronic coulomb interaction in $3d$ transition metal oxide perovskites, *Phys. Rev. B* **98**, 075130 (2018).
- [33] K. Kataoka, D. Hirai, T. Yajima, D. Nishio-Hamane, R. Ishii, K.-Y. Choi, D. Wulferding, P. Lemmens, S. Kitakata, T. Sakakibara, et al., Kitaev spin liquid candidate Os_xCl_3 comprised of honeycomb nano-domains, *Journal of the Physical Society of Japan* **89**, 114709 (2020).
- [34] X.-L. Sheng and B. K. Nikolić, Monolayer of the $5d$ transition metal trichloride OsCl_3 : A playground for two-dimensional magnetism, room-temperature quantum anomalous hall effect, and topological phase transitions, *Phys. Rev. B* **95**, 201402 (2017).
- [35] S. M. Winter, Y. Li, H. O. Jeschke, and R. Valentí, Challenges in design of Kitaev materials: Magnetic interactions from competing energy scales, *Phys. Rev. B* **93**, 214431 (2016).
- [36] J. G. Rau, E. K.-H. Lee, and H.-Y. Kee, Spin-orbit physics giving rise to novel phases in correlated systems: Iridates and related materials, *Annual Review of Condensed Matter Physics* **7**, 195 (2016).
- [37] S. K. Pandey, Q. Gu, Y. Lin, R. Tiwari, and J. Feng, Emergence of bond-dependent highly anisotropic magnetic interactions in sr_4rho_6 : A theoretical study, *Phys. Rev. B* **107**, 115119 (2023).
- [38] P. H. Souza, D. P. d. A. Deus, W. H. Brito, and R. H. Miwa, Magnetic anisotropy energies and metal-insulator transitions in monolayers of $\alpha\text{-RuCl}_3$ and OsCl_3 on graphene, *Phys. Rev. B* **106**, 155118 (2022).
- [39] Q. Gu, S. K. Pandey, and Y. Lin, For crystal structure, methodology, phonon dispersion, magnetic anisotropy plot, validity of $j_{\text{eff}} = 1/2$ picture and spin-wave spectra, refer to the supplemental material. (2023).
- [40] K. Hu, F. Wang, and J. Feng, First-principles study of the magnetic structure of Na_2IrO_3 , *Phys. Rev. Lett.* **115**, 167204 (2015).
- [41] S. Hwan Chun, J.-W. Kim, J. Kim, H. Zheng, C. C. Stoumpos, C. Malliakas, J. Mitchell, K. Mehlawat, Y. Singh, Y. Choi, et al., Direct evidence for dominant bond-directional interactions in a honeycomb lattice iridate Na_2IrO_3 , *Nat. Phys.* **11**, 462 (2015).
- [42] S. Middey, A. K. Nandy, S. Pandey, P. Mahadevan, and D. Sarma, Route to high néel temperatures in $4d$ and $5d$ transition metal oxides, *Phys. Rev. B* **86**, 104406 (2012).
- [43] S. K. Pandey, P. Mahadevan, and D. D. Sarma, Doping an antiferromagnetic insulator: A route to an antiferromagnetic metallic phase, *Europhysics Letters* **117**, 57003 (2017).
- [44] J. Reuther, R. Thomale, and S. Trebst, Finite-temperature phase diagram of the heisenberg-kitaev model, *Phys. Rev. B* **84**, 100406 (2011); R. Suttner, C. Platt, J. Reuther, and R. Thomale, Renormalization group analysis of competing quantum phases in the $J_1\text{-}J_2$ heisenberg model on the kagome lattice, *Phys. Rev. B* **89**, 020408 (2014); M. Hering, F. Ferrari, A. Razpopov, I. I. Mazin, R. Valentí, H. O. Jeschke, and J. Reuther, Phase diagram of a distorted kagome antiferromagnet and application to y-kapellasite, *npj Computational Materials* **8**, 10 (2022).
- [45] N. Astrakhantsev, F. Ferrari, N. Niggemann, T. Müller, A. Chauhan, A. Kshetrimayum, P. Ghosh, N. Regnault, R. Thomale, J. Reuther, T. Neupert, and Y. Iqbal, Pinwheel valence bond crystal ground state of the spin- $\frac{1}{2}$ heisenberg antiferromagnet on the shuriken lattice, *Phys. Rev. B* **104**, L220408 (2021); Y. Iqbal, H. O. Jeschke, J. Reuther, R. Valentí, I. I. Mazin, M. Greiter, and R. Thomale, Paramagnetism in the kagome compounds $(\text{Zn,Mg,Cd})\text{Cu}_3(\text{OH})_6\text{Cl}_2$, *Phys. Rev. B* **92**, 220404 (2015); Y. Watanabe, S. Trebst, and C. Hickey, Frustrated ferromagnetism of honeycomb cobaltates: Incommensurate spirals, quantum disordered phases, and out-of-plane ising order (2022), [arXiv:2212.14053 \[cond-mat.str-el\]](https://arxiv.org/abs/2212.14053).
- [46] G. Kresse and D. Joubert, From ultrasoft pseudopotentials to the projector augmented-wave method, *Phys. Rev. B* **59**, 1758 (1999).
- [47] P. E. Blöchl, Projector augmented-wave method, *Phys. Rev. B* **50**, 17953 (1994).
- [48] G. Kresse and J. Hafner, Ab initio molecular dynamics for liquid metals, *Phys. Rev. B* **47**, 558 (1993).
- [49] G. Kresse and J. Furthmüller, Efficiency of ab-initio total energy calculations for metals and semiconductors using a plane-wave basis set, *Comput. Mater. Sci.* **6**, 15 (1996).
- [50] G. Kresse and J. Furthmüller, Efficient iterative schemes

- for ab initio total-energy calculations using a plane-wave basis set, *Phys. Rev. B* **54**, 11169 (1996).
- [51] J. P. Perdew, K. Burke, and M. Ernzerhof, Generalized gradient approximation made simple, *Phys. Rev. Lett.* **77**, 3865 (1996).
- [52] S. L. Dudarev, G. A. Botton, S. Y. Savrasov, C. J. Humphreys, and A. P. Sutton, Electron-energy-loss spectra and the structural stability of nickel oxide: An LSDA+U study, *Phys. Rev. B* **57**, 1505 (1998).
- [53] A. Togo and I. Tanaka, First principles phonon calculations in materials science, *Scr. Mater.* **108**, 1 (2015).
- [54] A. Togo, First-principles phonon calculations with phonopy and phono3py, *J. Phys. Soc. Jpn.* **92**, 012001 (2023).
- [55] A. A. Mostofi, J. R. Yates, Y.-S. Lee, I. Souza, D. Vanderbilt, and N. Marzari, wannier90: A tool for obtaining maximally-localised Wannier functions, *Comput. Phys. Commun.* **178**, 685 (2008).
- [56] C. Franchini, R. Kovacik, M. Marsman, S. S. Murthy, J. He, C. Ederer, and G. Kresse, Maximally localized Wannier functions in LaMnO₃ within PBE+U, hybrid functionals and partially self-consistent GW: an efficient route to construct *ab initio* tight-binding parameters for e_g perovskites, *Journal of Physics: Condensed Matter* **24**, 235602 (2012).
- [57] Q. Gu, S. K. Pandey, and R. Tiwari, A computational method to estimate spin-orbital interaction strength in solid state systems, *Comput. Mater. Sci.* **221**, 112090 (2023).
- [58] S. L. Adler, Quantum theory of the dielectric constant in real solids, *Phys. Rev.* **126**, 413 (1962).
- [59] N. Wiser, Dielectric constant with local field effects included, *Phys. Rev.* **129**, 62 (1963).
- [60] F. Aryasetiawan, M. Imada, A. Georges, G. Kotliar, S. Biermann, and A. I. Lichtenstein, Frequency-dependent local interactions and low-energy effective models from electronic structure calculations, *Phys. Rev. B* **70**, 195104 (2004).
- [61] F. L. Buessen, The SpinParser software for pseudofermion functional renormalization group calculations on quantum magnets, *SciPost Phys. Codebases* , 5 (2022).
- [62] J. Reuther and P. Wölfle, J_1 – J_2 frustrated two-dimensional heisenberg model: Random phase approximation and functional renormalization group, *Phys. Rev. B* **81**, 144410 (2010).
- [63] F. L. Buessen, V. Noculak, S. Trebst, and J. Reuther, Functional renormalization group for frustrated magnets with nondiagonal spin interactions, *Phys. Rev. B* **100**, 125164 (2019).
- [64] S. Toth and B. Lake, Linear spin wave theory for single-q incommensurate magnetic structures, *J. Phys.: Condens. Matter* **27**, 166002 (2015).

SUPPLEMENTARY MATERIALS

1. *Ab initio* calculations

a. Details of *ab initio* calculations

Density-functional theory (DFT) calculations have been performed using projector-augmented wave method [46, 47], implemented within Vienna *ab initio* simulation package (VASP) [48–50]. The Perdew-Burke-Ernzerhof functional [51] is used for the exchange-correlation functional within the GGA formalism. We start with the monoclinic ($C2/m$) crystal structure for the monolayer OsCl_3 with 2 Os atom unit cell as shown in Fig. S1(a). Full structural relaxation is performed on the $2 \times 1 \times 1$ magnetic supercell with FM and ZZ magnetic orders (shown in Fig. S1(b)). The energy cutoff for a plane-wave basis is set to 500 eV and Γ -centered k -mesh of $4 \times 8 \times 1$ is considered in our calculations. High accuracy of our calculations is ensured by tighter relaxation convergence criterion wherein tolerance considered for total energy is 10^{-8} eV while for force it is 5×10^{-6} eV/Å. Full optimization of crystal structure is performed after considering $U = 1$ eV under Dudarev [52] scheme and spin-orbit coupling (SOC) effect at the self-consistent level. For both the cases of ZZ and FM states, optimization resulted in the similar crystal structure and optimized lattice constants are $a = b = 6.1787$ Å, vacuum $c = 25$ Å, and $\alpha = \beta = 90^\circ$ and $\gamma \approx 120^\circ$ and atomic coordinates of the final structure are listed in the Table S1. The primitive unit cell is shown in Fig. S1 (a) and Brillouin zone (BZ) for the zigzag (ZZ) supercell is shown in Fig. S1 (c).

TABLE S1. Atomic coordinates in magnetic unit cell of monolayer OsCl_3 with space group $C2/m$. Lattice constants are $a = b = 6.1787$ Å, $c = 25$ Å, $\alpha = \beta = 90^\circ$ and $\gamma = 119.88^\circ$

atom	x/a	y/b	z/c
Os1	0.166797	0.833203	0.500000
Os2	0.833203	0.166797	0.500000
Cl1	0.855480	0.855480	0.446984
Cl2	0.144520	0.144520	0.553016
Cl3	0.499663	0.143222	0.446932
Cl4	0.856778	0.500337	0.553068
Cl5	0.500337	0.856778	0.553068
Cl6	0.143222	0.499663	0.446932

b. Phonon dispersion

The pristine monolayer OsCl_3 has not been observed experimentally yet. As explained in the main text, triangular lattice of Os^{+3} ions with nanometer sized honeycomb domains is observed recently in experiments [33]. This raises a natural question about the structural stability of the resulting monolayer honeycomb lattice. To answer this, we perform phonon calculations on a $2 \times 4 \times 1$

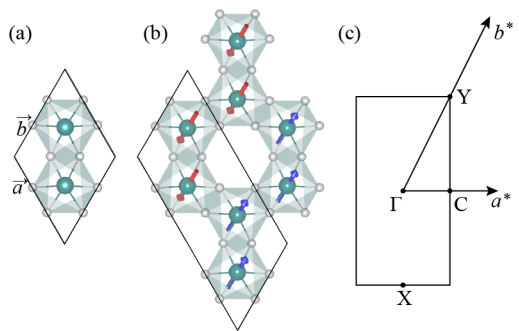


FIG. S1. (a) Primitive unit cell of OsCl_3 , (b) the $2 \times 1 \times 1$ supercell hosting ZZ magnetic order, and (c) BZ of the ZZ supercell.

supercell, while considering Hubbard $U = 1$ eV on Os d orbitals and imposing ZZ magnetic configuration. We used the finite displacement method to calculate the force constants and phonon dispersions obtained with and without SOC effects are shown in Fig. S2. In both cases, crystal structure is at least dynamically stable as no soft modes are found in our calculations. The post-processing of these phonon calculation is done by Phonopy package [53, 54].

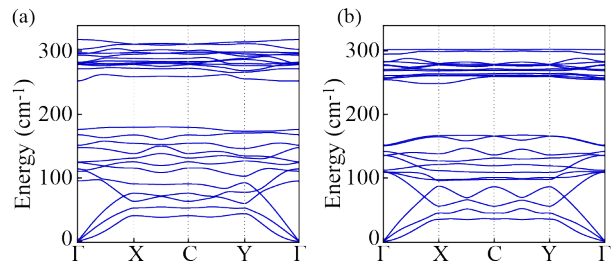


FIG. S2. Phonon dispersion plots for monolayer OsCl_3 with ZZ magnetic order and $U = 1$ eV on Os d orbitals calculated without (a) and with (b) SOC effect.

c. In-plane magnetic anisotropy

To obtain the magnetic anisotropy in monolayer OsCl_3 , we start with magnetic moments aligned along \mathbf{a} axis in the FM state. We then rotate these moments by 30° in the \mathbf{ab} plane and perform total energy calculations. Upper limit of rotation was fixed at 180° . Obviously, at 120° , magnetic moments are aligned along the \mathbf{b} axis. Obtained plot is shown in Fig. S3. From this plot, one can conclude that while Os spins prefer to align along \mathbf{a} axis, the in-plane anisotropic energy is small in monolayer OsCl_3 .

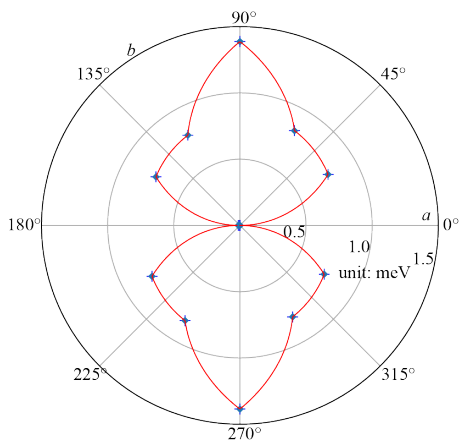


FIG. S3. In-plane magnetic anisotropy in monolayer OsCl_3 estimated considering FM state. While Os spins prefer to align along \mathbf{a} , in-plane magnetic anisotropy is small in this material.

2. Estimation of electronic parameters

a. Crystal field splitting and hopping amplitudes

Crystal field matrix and hopping amplitudes are estimated from a non spin-polarised, SOC excluded tight-binding (H_{TB}) Hamiltonian expressed in the local axes framework depicted in Fig. 1(a). These two terms can be given as,

$$H_{\text{TB}} = H_{\text{cf}} + H_{\text{hop}}$$

The above Hamiltonian can be obtained by projecting the *ab initio* band structure onto a Wannier functions in which all the five Os- d orbitals form the basis [55, 56]. The choice of the local axes (\mathbf{x} , \mathbf{y} , \mathbf{z}) in Fig. 1(a) along the oxygen atoms is such that $\mathbf{c} = \mathbf{x} + \mathbf{y} + \mathbf{z}$ lies along trigonal distortion axis of the OsCl_6 octahedra. Close agreement between thus obtained TB model and *ab initio* band structure is shown in Fig. S4(a). Crystal field matrix on a site i (Δ_i^{CF}) in the above term H_{cf} is extracted from the onsite part of H_{TB} and is given by,

$$\Delta_i^{\text{CF}} = \begin{bmatrix} 2.6322 & -0.0772 & 0.2578 & -0.0122 & 0.0369 \\ -0.0772 & 0.0479 & -0.0268 & 0.0709 & 0.0272 \\ 0.2578 & -0.0268 & 0.0707 & 0.1026 & 0.0366 \\ -0.0122 & 0.0709 & 0.1026 & 2.6244 & 0.2800 \\ 0.0369 & 0.0272 & 0.0366 & 0.2800 & 0.0748 \end{bmatrix} \quad (\text{S1})$$

Entries in the above matrix are in eV. Hopping amplitudes up to third neighbor are listed below in Table S2.

b. Estimation of SOC strength (λ)

To extract SOC strength in OsCl_3 , we added an onsite SOC term to the TB Hamiltonian as[57],

$$H = \mathcal{I}_2 \otimes H_{\text{TB}} + H_{\text{soc}}$$

where \mathcal{I}_2 is the two-dimensional identity matrix and \otimes is the Kronecker product. $H_{\text{soc}} = \sum_i \lambda \mathbf{L}_i \cdot \mathbf{s}_i$ is the onsite SOC interaction term that couples the electronic spin (\mathbf{S}) and its orbital momentum (\mathbf{L}) with a strength λ . Here, the SOC strength λ is estimated by fitting the eigenvalues of H with those obtained from SOC included *ab initio* band structure calculations as the target. The best agreement between these two band structures, shown in Fig. S4(b), is obtained for $\lambda = 0.335$ eV which is considered in further calculations.

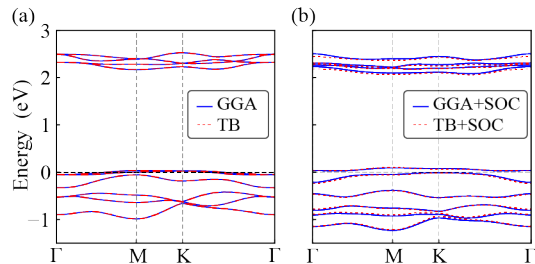


FIG. S4. Comparison of *ab initio* and TB model band structures for, (a) non spin-polarized case, and (b) SOC included case. In (b), SOC effects in *ab initio* calculations are included self-consistently, which then fitted with the TB Hamiltonian obtained in (a) after explicitly adding onsite SOC term $H_{\text{soc}} = \sum_i \lambda \mathbf{L}_i \cdot \mathbf{s}_i$ to H_{TB} .

c. Estimation of Hubbard U and Hund's J_H within cRPA

We estimate the Coulomb matrix elements $U_{ijkl}(\omega = 0)$ within the constrained random phase approximation (cRPA) implemented with VASP [58–60]. We neglect the screening effects for all the five Os d orbital states which are energetically well-separated from other states (see Fig. S4). The estimated parameters are $U = 3.8$ eV and $J_H = 0.141$ eV.

3. Validity of $j_{\text{eff}} = 1/2$ picture

It is crucial to analyse the effects of various electronic interaction on the band structure of monolayer OsCl_3 . Such analysis can help us to examine the validity of low-energy $j_{\text{eff}} = 1/2$ picture, which is considered as a building block for emergence of dominant Kitaev interaction. To this end *ab initio* band structure calculations are performed for three cases, *viz* SOC, SOC + U and SOC + U + ZZ magnetic state. Obtained results are then projected onto $j_{\text{eff}} = 1/2$ and $3/2$ states, eigenfunctions of which are given below in Eq. S2.

TABLE S2. First, second and third neighbor Os-Os hopping amplitudes (in eV) on different types of bonds listed in the basis $\psi^\dagger = [d_{z^2}^\dagger, d_{xz}^\dagger, d_{yz}^\dagger, d_{x^2-y^2}^\dagger, d_{xy}^\dagger]$

X ₁ -bond	Y ₁ -bond	Z ₁ -bond
$\begin{pmatrix} -0.0158 & -0.0435 & -0.0167 & -0.0216 & 0.2056 \\ -0.0435 & 0.0153 & 0.1882 & -0.0195 & 0.0178 \\ -0.0167 & 0.1882 & 0.0563 & -0.0039 & 0.0544 \\ -0.0216 & -0.0195 & -0.0039 & 0.0111 & 0.0073 \\ 0.2056 & 0.0178 & 0.0544 & 0.0073 & -0.0712 \end{pmatrix}$	$\begin{pmatrix} -0.0149 & 0.0029 & 0.1102 & 0.0255 & -0.0236 \\ 0.0029 & 0.0602 & -0.0316 & 0.0118 & -0.1922 \\ 0.1102 & -0.0316 & -0.0754 & -0.1784 & -0.005 \\ 0.0255 & 0.0118 & -0.1784 & 0.0065 & 0.0162 \\ -0.0236 & -0.1922 & -0.0050 & 0.0162 & 0.0192 \end{pmatrix}$	$\begin{pmatrix} 0.0104 & 0.1021 & 0.0049 & -0.0100 & 0.0081 \\ 0.1021 & -0.0785 & -0.0007 & 0.1768 & 0.0485 \\ 0.0049 & -0.0007 & 0.0332 & 0.0459 & -0.1883 \\ -0.0100 & 0.1768 & 0.0459 & -0.0180 & 0.0003 \\ 0.0081 & 0.0485 & -0.1883 & 0.0003 & 0.0479 \end{pmatrix}$
X ₂ -bond	Y ₂ -bond	Z ₂ -bond
$\begin{pmatrix} 0.0156 & 0.0709 & -0.0418 & 0.0218 & -0.007 \\ 0.0360 & 0.0009 & 0.0132 & 0.0938 & 0.0149 \\ -0.0394 & 0.0041 & -0.015 & -0.0098 & 0.0467 \\ 0.0082 & 0.0776 & -0.0184 & 0.0013 & 0.0475 \\ -0.0091 & 0.0018 & 0.0512 & 0.0556 & 0.0016 \end{pmatrix}$	$\begin{pmatrix} 0.0133 & 0.0276 & 0.0428 & -0.0235 & 0.0971 \\ 0.036 & -0.0056 & -0.0501 & -0.0289 & -0.0115 \\ 0.0372 & -0.0462 & -0.0024 & 0.0269 & 0.0164 \\ -0.0107 & -0.0310 & 0.0324 & -0.0025 & 0.0160 \\ 0.1009 & -0.0007 & 0.0047 & -0.0220 & 0.0016 \end{pmatrix}$	$\begin{pmatrix} -0.0082 & -0.0430 & 0.0304 & 0.0061 & -0.0084 \\ -0.0513 & -0.0088 & -0.0009 & 0.0189 & 0.0528 \\ 0.0624 & -0.0120 & 0.0016 & -0.0741 & -0.0140 \\ -0.0066 & 0.0164 & -0.0957 & 0.0316 & -0.0453 \\ -0.0135 & 0.0474 & -0.0052 & -0.0387 & -0.0121 \end{pmatrix}$
X ₃ -bond	Y ₃ -bond	Z ₃ -bond
$\begin{pmatrix} 0.0296 & 0.0087 & 0.0008 & -0.0299 & 0.0050 \\ 0.0087 & -0.0312 & 0.0065 & 0.0237 & -0.0083 \\ 0.0008 & 0.0065 & 0.0091 & -0.0146 & 0.0120 \\ -0.0299 & 0.0237 & -0.0146 & -0.0074 & 0.0050 \\ 0.005 & -0.0083 & 0.0120 & 0.0050 & 0.0090 \end{pmatrix}$	$\begin{pmatrix} -0.0252 & 0.0101 & 0.0073 & -0.0028 & 0.0248 \\ 0.0101 & 0.0108 & -0.0111 & 0.0069 & -0.0048 \\ 0.0073 & -0.0111 & 0.0088 & -0.0012 & -0.0070 \\ -0.0028 & 0.0069 & -0.0012 & 0.0460 & 0.0083 \\ 0.0248 & -0.0048 & -0.0070 & 0.0083 & -0.0304 \end{pmatrix}$	$\begin{pmatrix} 0.0258 & -0.0029 & 0.0202 & 0.0307 & 0.0128 \\ -0.0029 & 0.0075 & 0.0097 & 0.009 & 0.0131 \\ 0.0202 & 0.0097 & -0.029 & -0.0153 & -0.0067 \\ 0.0307 & 0.009 & -0.0153 & -0.0037 & -0.0068 \\ 0.0128 & 0.0131 & -0.0067 & -0.0068 & 0.0093 \end{pmatrix}$

$$\begin{aligned}
\left| \frac{1}{2}, \pm \frac{1}{2} \right\rangle &= \frac{1}{\sqrt{3}} \left(\mp |d_{xy}; \pm \frac{1}{2}\rangle \mp i |d_{xz}; \mp \frac{1}{2}\rangle - |d_{yz}; \mp \frac{1}{2}\rangle \right) \\
\left| \frac{3}{2}, \pm \frac{3}{2} \right\rangle &= \frac{1}{\sqrt{2}} \left(-i |d_{xz}; \pm \frac{1}{2}\rangle \mp |d_{yz}; \pm \frac{1}{2}\rangle \right) \\
\left| \frac{3}{2}, \pm \frac{1}{2} \right\rangle &= \frac{1}{\sqrt{6}} \left(2 |d_{xy}; \pm \frac{1}{2}\rangle - i |d_{xz}; \mp \frac{1}{2}\rangle \mp |d_{yz}; \mp \frac{1}{2}\rangle \right)
\end{aligned} \tag{S2}$$

Plots obtained for the three cases are shown in Fig. S5(a), (b) and (c) respectively. SOC effect is included at the self-consistent level in all these calculations.

Certain features of the band structures can immediately be identified. Firstly, one can find a clear separation between narrow $j_{\text{eff}} = 1/2$ and $3/2$ bands for SOC-only band structure shown in Fig. S5(a). In Fig. S5(b), for the SOC + U case, the $j_{\text{eff}} = 1/2$ bands near the Fermi level remain largely unaffected at this $U = 1$ eV (though a larger $U = 2$ eV opens a clear band gap which is not shown here) and system is nearly insulating in both the cases. This differs from the α -RuCl₃ picture presented by Kim *et al.* [6] where $U = 1.5$ eV was necessary to bring out a clear $j_{\text{eff}} = 1/2$ - $3/2$ separation and to drive the system insulating. The weak response towards smaller U along with the narrow bandwidth (~ 0.3 eV) of $j_{\text{eff}} = 1/2$ states may be hinting that t and U parameters have similar scale in this material. A constrained random phase approximation (cRPA) estimation brings $U = 3.8$ eV and $J_{\text{H}} = 0.143$ eV for monolayer OsCl₃. However, the largest 1NN hopping magnitude $|t|$ estimated from the Wannier TB model is ≈ 0.2 eV. Based on these values, one can still think of limit $t \ll U$ and hence formation of well-localized j_{eff} states in this compound. A wider band gap opens up once magnetism in the form of ZZ state is included and obtained band structure for this case is shown in Fig. S5(c).

4. Second-order perturbation method

The full Hamiltonian for the d^5 Os⁺³ ions is given by,

$$\mathcal{H} = H_{\text{hop}} + H_{\text{cf}} + H_{\text{soc}} + H_{\text{int}} \tag{S3}$$

where the terms in the right hand side are hopping, CF, SOC and Hubbard-Kanamori interaction Hamiltonians. Using the basis $\psi_{i\sigma}^\dagger = [d_{z^2}^\dagger, d_{xz}^\dagger, d_{yz}^\dagger, d_{x^2-y^2}^\dagger, d_{xy}^\dagger]_{i\sigma}$ at site i of Os and spin σ , above Hamiltonian then reads,

$$\begin{aligned}
\mathcal{H} &= \sum_{i \neq j, \sigma} \psi_{i\sigma}^\dagger T_{ij} \psi_{j\sigma} + \sum_{i, \sigma} \psi_{i\sigma}^\dagger \Delta_i^{\text{CF}} \psi_{i\sigma} + \sum_i \lambda \mathbf{L}_i \cdot \mathbf{s}_i \\
&+ \frac{U}{2} \sum_{i, \alpha} n_{i\alpha\sigma} n_{i\alpha\sigma'} + \frac{U'}{2} \sum_{i, \alpha \neq \beta} n_{i\alpha} n_{i\beta} \\
&- \frac{J_{\text{H}}}{2} \sum_{i, \sigma, \sigma', \alpha \neq \beta} \psi_{i\alpha\sigma}^\dagger \psi_{i\alpha\sigma'} \psi_{i\beta\sigma'}^\dagger \psi_{i\beta\sigma} \\
&- \frac{J'}{2} \sum_{i, \sigma \neq \sigma', \alpha \neq \beta} \psi_{i\alpha\sigma}^\dagger \psi_{i\beta\sigma'} \psi_{i\alpha\sigma'}^\dagger \psi_{i\beta\sigma}
\end{aligned} \tag{S4}$$

In above expression, the first three terms are hoppings, CF and SOC, while the last four terms are the Hubbard-Kanamori interactions. The U/U' are intra-orbital/interorbital Hartree energies and J_{H} and J' are Hund's coupling and pair hopping interaction, respectively. Rotational invariance in the isolated atom limit dictates the relationships: $U' = U - 2J_{\text{H}}$ and $J_{\text{H}} = J'$. Hopping amplitudes T_{ij} and CF matrix Δ_i^{CF} can be obtained by fitting the *ab initio* band structure with a TB model as described earlier.

In the limit $t \ll U$, i.e. in the isolated atom limit, one can separate the ‘‘onsite’’ term H_i^0 at a site i from \mathcal{H} as,

$$H_i^0 = H_{\text{cf}} + H_{\text{soc}} + H_{\text{int}}$$

We drop index i since this Hamiltonian is the same for each site. The key here is that d^5 manifold has a two-fold degenerate ground state, which form a Kramers doublet and can be treated as a pseudospin-1/2. In order to extract the magnetic interactions of these pseudospin states, we first project the full TB Hamiltonian onto the pseudospin $j_{1/2}$ space $\{\phi_{i\alpha}\}$, $\alpha = \uparrow, \downarrow$, where \uparrow, \downarrow refer to the SOC pseudospin-1/2 states. Starting from isolated limit we introduce H_{hop} as perturbation. In the second-order perturbation theory, the Hamiltonian is written as,

$$H^{(2)} = \sum_{ij} \sum_{\alpha\beta\alpha'\beta'} \mathcal{H}(i, j)_{\alpha\beta\alpha'\beta'} |i\alpha, j\beta\rangle \langle i\alpha', j\beta'|,$$

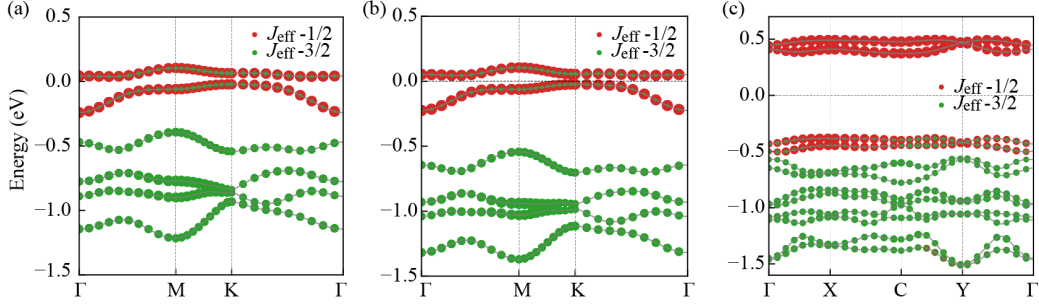


FIG. S5. Band structure plots of monolayer OsCl_3 for, (a) SOC included, (b) SOC + U , and (c) SOC + U + ZZ magnetic state are shown. Red and green spheres depicted weight of $j_{\text{eff}} = 1/2$ and $3/2$ states, respectively. Fermi energy is set to zero in these plots.

$$\mathcal{H}(i, j)_{\alpha\beta\alpha'\beta'} = \sum_{kl} \sum_{\gamma\lambda} \frac{1}{\Delta E} \langle i\alpha, j\beta | H_{\text{hop}} | k\gamma, l\lambda \rangle \times \langle k\gamma, l\lambda | H_{\text{hop}} | i\alpha', j\beta' \rangle, \quad (\text{S5})$$

where $1/\Delta E = \frac{1}{2}[1/(E_{i\alpha} + E_{j\beta} - E_{k\lambda} - E_{l\gamma}) + 1/(E_{i\alpha'} + E_{j\beta'} - E_{k\lambda} - E_{l\gamma})]$. Here, $|i\alpha, j\beta\rangle$ and $|i\alpha', j\beta'\rangle$ are two-site states in the $j_{\text{eff}} = 1/2$ ground states, and $|k\lambda, l\gamma\rangle$ are two-site excited states, both in the isolated atom limit. H_{hop} connects a two-site ground state to an excited state with (d^4, d^6) configuration, the dimensions of whose Hilbert spaces is 210. The eigenstates of isolated Os with 4, 5 and 6 d electrons are obtained by exact diagonalization. One can represent the pseudo-spins $j_{1/2}$ as $S^\mu = \langle i\alpha | j_{i,\text{eff}}^\mu | i\beta \rangle$ which are the expectation values of pseudospin j_{eff}^μ operators with $\mu = 0, x, y, z$. Here, $j_{\text{eff}}^0 = \mathcal{I}_2$ is the matrix representation of operator j_{eff}^0 . Eq. (S5) can be mapped to a spin Hamiltonian of the form,

$$H_{\text{spin}} = S_i^\mu \eta(i, j)^{\mu\nu} S_j^\nu = \frac{1}{4} \eta(i, j)^{\mu\nu} \phi_{i\alpha}^\dagger \sigma_{\alpha\alpha'}^\mu \phi_{i\alpha'} \phi_{j\beta} \sigma_{\beta\beta'}^\nu \phi_{j\beta'}^\dagger, \quad (\text{S6})$$

where $\mu, \nu = 0, x, y, z$, σ^μ are Pauli matrices, and summation over all repeated indexes is implied. The map can be achieved by solving the linear equations

$$-\frac{1}{4} \sigma_{\alpha\alpha'}^\mu \sigma_{\beta\beta'}^\nu \eta(ij)^{\mu\nu} = \mathcal{H}(i, j)_{\alpha\beta\alpha'\beta'} \quad (\text{S7})$$

Thus, the most general form of exchange interaction matrix on the three Os-Os bonds can be written as,

$$\begin{aligned} \eta_X &= \begin{pmatrix} J+K & \Gamma'+\zeta & \Gamma'-\zeta \\ \Gamma'+\zeta & J+\xi & \Gamma \\ \Gamma'-\zeta & \Gamma & J-\xi \end{pmatrix} \\ \eta_Y &= \begin{pmatrix} J+\xi & \Gamma'+\zeta & \Gamma \\ \Gamma'+\zeta & J+K & \Gamma'-\zeta \\ \Gamma & \Gamma'-\zeta & J-\xi \end{pmatrix} \\ \eta_Z &= \begin{pmatrix} J+\xi & \Gamma & \Gamma'+\zeta \\ \Gamma & J-\xi & \Gamma'-\zeta \\ \Gamma'+\zeta & \Gamma'-\zeta & J+K \end{pmatrix} \end{aligned} \quad (\text{S8})$$

Only these symmetric components of interaction matrices appear on the first and third neighbor bonds, while on the second neighbor bonds, due to absence of inversion symmetry, additional antisymmetric component appears in the form of Dzyaloshinskii–Moriya interaction (DMI). The matrix from of these antisymmetric interaction is given in Ref. [35].

5. Pseudofermion functional renormalization group calculations

We use SpinParser package [61] to perform pseudofermion functional renormalization group (pf-FRG) calculations [62, 63] on generalized Kitaev spin model obtained in the previous section. We consider heoneycomb lattice to initialize vertex functions in order to capture two-particle interactions on lattice sites separated up to 7 lattice bonds. In pf-FRG calculations, the single-particle vertex $\Sigma^\Lambda(\omega)$ and two-particle vertex basis functions $\Gamma^\Lambda(\omega, \omega', \omega'')$ are parameterized by a frequencies ω and the renormalization group cutoff Λ . Here, the we use a logarithmically spaced mesh of discrete frequencies as

$$\omega_n = \omega_{\min} \left(\frac{\omega_{\max}}{\omega_{\min}} \right)^{\frac{n}{N_\omega - 1}}; \quad n = (0, 1, \dots, N_\omega - 1).$$

where ω_{\min} and ω_{\max} are the limit points of frequency on the positive half-axis which are set to be 0.01 and 35.0 respectively. N_ω is the overall number of positive frequencies and chosen to be 32 in our case. As for the negative half-axis, the frequencies are generated automatically by symmetry. The discretization of the cutoff parameter Λ is also done on a logarithmically spaced mesh given by,

$$\Lambda_n = \Lambda_{\max} b^n; \quad n = 0, \dots, \left\lfloor \log_b \left(\frac{\Lambda_{\min}}{\Lambda_{\max}} \right) \right\rfloor$$

where the Λ_{\min} and Λ_{\max} are the lower and upper boundaries of Λ which are set to be 0.01 and 50, respectively. The parameter b is step size and set to be 0.98 in our calculations. Though we have considered up to 3NN interactions in our pf-FRG calculations, negligibly small 2NN

and 3NN magnetic interactions does not affect the magnetic ground state obtained with this method at qualitative level. We find that most part of the phase points in Fig. 2(a) of the main text can be described by dominant 1NN magnetic interactions only.

6. Atomic features

One of the quantities which can be measured from the resonant inelastic X-ray scattering (RIXS) experiments are the single-point excitations represented by sharp peaks in the scattering intensity in the relevant energy range. It can be a direct probe for cubic symmetry lowering of the Rh-O₆ octahedra in a material. Theoretically, such a low-lying crystal field-assisted many-body excitations bear a close resemblance with the eigenvalues obtained from diagonalization of many-body “onsite” Hamiltonian H^0 . Hence, we discuss here the nature of CF splitting in monolayer OsCl₃ and its effect on electronic structure. The CF matrix is given in Eq. S1.

Examining eigenvalues of CF matrix (Δ_i) in Eq. S1 reveals that $t_{2g-e_g} \Delta_i^{t_{2g}-e_g} \approx 2.60$ eV and there is additional trigonal distortion $\Delta_i^{\text{tri}} \approx 64$ meV of the octahedra. Eigenvalues obtained after exact diagonalization of H_i^0 with this Δ_i^{CF} can be compared with the single-point excitations observed in RIXS experiments. In our calculation, we find $j_{\text{eff}} = 1/2 - 3/2$ separation to be 0.580 eV which is approximately $\frac{3}{2}\lambda$ for $\lambda = 0.355$ eV estimated from band structure fitting of monolayer OsCl₃. The four fold $j_{\text{eff}} = 3/2$ states split into two doublets which are separated by ≈ 56 meV. This splitting is a direct consequence of Δ_i^{tri} present and is also found Iridates and α -RuCl₃. By putting $\Delta_i^{\text{tri}} = 0$ eV, as expected, $j_{\text{eff}} = 3/2$ states regained the four fold degeneracy.

7. Magnetic interaction and ground state from cRPA parameters

Below in Table S3, we provide estimated magnetic interactions corresponding to parameters obtained from cRPA, i.e. $U = 3.8$ eV and $J_{\text{H}} = 0.143$ eV.

We use these interactions from Table S3 in the pf-FRG calculations and the static spin correlation for the corresponding ZZ ground state is shown in Fig. S6. One of the M point of first BZ contributes to this ground state indicating some sort of “anisotropic” ZZ state.

8. Quantitatively different zigzag states in phase diagram

As we have mentioned that different part of the phase diagram in Fig. 2(a) of the main text hosts different magnetic ground state depending upon the nature of dominant magnetic interactions. The largest part of the phase diagram is occupied by ZZ magnetic state which differ

TABLE S3. Estimated bond-dependent magnetic interactions for cRPA estimated $U = 3.8$ eV, $J_{\text{H}} = 0.143$ eV. Here also, $\lambda = 0.355$ eV. Values of Heisenberg J , Kitaev K , off-diagonal Γ , and Γ' terms along with diagonal and off-diagonal anisotropic terms ξ and ζ are listed. 3NN interactions as well as some 2NN interactions are < 0.05 meV and hence not listed here.

Bond	Magnetic interactions (meV)					
	J	K	Γ	Γ'	ξ	ζ
X ₁	0.133	-1.824	-5.711	0.858	1.342	-1.940
Y ₁	0.130	-19.203	-5.755	-1.096	-0.767	-2.577
Z ₁	0.100	-19.214	5.299	3.516	-1.295	0.382
X ₂	-0.211	0.573	-0.137	-0.056	-	-0.088
Y ₂	-0.230	0.633	-0.126	0.074	-	-0.167
Z ₂	-0.234	0.636	0.115	0.144	-	0.061
D_{ij}						
X ₂	$< 0.04 $					
Y ₂	$< 0.04 $					
Z ₂	$< 0.04 $					

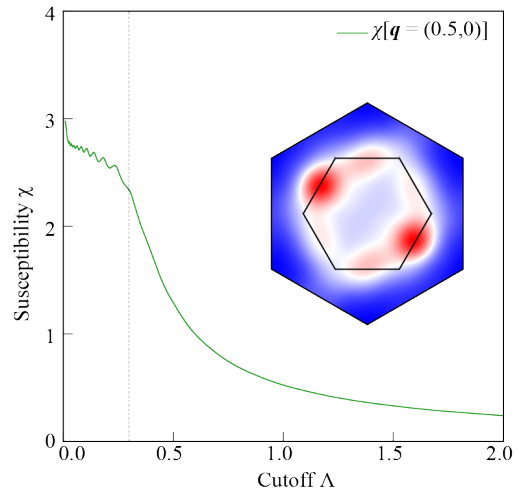


FIG. S6. Static spin correlations plot, shown in inset, obtained from pf-FRG calculations using magnetic interactions from Table S3. Intensity contribution from one of the M point of the BZ indicates a ZZ ground state. The renormalization group flow of the magnetic correlation (χ) represented by green curve breaks at ≈ 0.3 Λ indicating the onset of the long-range magnetic order.

quantitatively in different regions of the phase space. To demonstrate this point, we plot two of them in Fig. S7. Spin orientations in these two ZZ states are obtained by optimization of classical ground state using SpinW package [64]. As one can see that in Fig. S7(a), spin alignment is in-plane while spins are tilted in out-of-plane direction in Fig. S7(b). In-plane configuration corresponds to $J = 0.4$ meV and $K = -18.2$ meV and out-of-plane configuration is obtained from interactions listed in Table S3. Corresponding spin-wave spectrum, calculated using linear spin-wave theory as implemented in SpinW [64], are

also shown in Fig. S7(c) and (d).

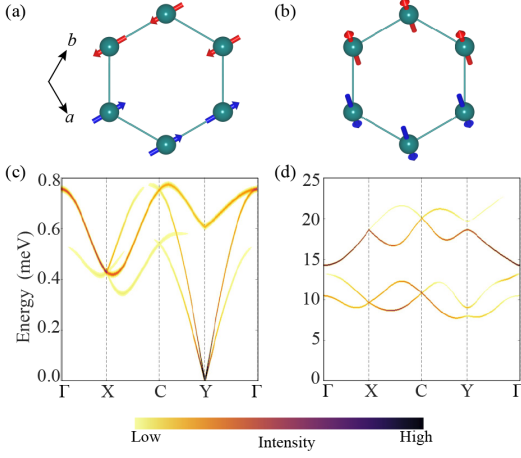


FIG. S7. Optimized classical magnetic ground states for interactions corresponding to, (a) $J = 0.4$ meV and $K = -18.2$ meV, and (b) interaction listed in Table S3. Spin wave spectra obtained using linear spin wave theory for, (c) in-plane configuration shown in (a), and (d) out-of-plane shown in (b)

As one can see that the spectra is gapless in Fig. S7(c) for the in-plane alignment of spins and is gapped in Fig. S7(d) for the out-of-plane tilting of spins. This distinctive feature of the spectra can be understood as follows. In absence of magnetic couplings like Γ and Γ' , any in-plane spin alignment would classically have same energy resulting in a gapless mode. This can be seen for the spin alignment of Fig. S7(a) results in a gapless mode at Y point. However, Γ and Γ' terms dictate the out-of-plane tilting of spins and pinning down of moments in a specific direction (along one of the Cl-Cl edges in Os-Cl_6 octahedra, see Fig. 1 (a)). This introduces additional anisotropy in the Hamiltonian causing the spectra to be gapped. Diagonal anisotropic term ξ may lead to further anisotropy in the system, in-turn actively contributing to a gapped spectra.